J Mater Sci: Mater Electron (2020) 31:21467–21477

Dielectric and ferroelectric properties of $(Bi_{0.5}Na_{0.5})_{0.94-\delta}Ba_{0.06}Ti_{1-x}Nb_xO_3$ lead-free ceramics

Han-li Lian[1,*], Jin-yan Shi[1], Yan-zi Qiu[2], and Xiao-ming Chen[2]

[1] School of Science, Xi'an University of Posts and Telecommunications, Xi'an 710121, People's Republic of China
[2] School of Physics and Information Technology, Shaanxi Normal University, Xi'an 710119, People's Republic of China

Received: 24 May 2020
Accepted: 12 October 2020
Published online: 23 October 2020

ABSTRACT

Lead-free ceramics $(Bi_{0.5}Na_{0.5})_{0.94-\delta}Ba_{0.06}Ti_{1-x}Nb_xO_3$ (x = 0, 0.01, 0.02, 0.03, 0.04, 0.05) were prepared via a solid-state sintering method. The ceramics exhibit pure perovskite structure as $x \leq 0.04$, while the ceramic with $x = 0.05$ has a secondary phase. The rhombohedral (R)–tetragonal (T) morphotropic phase boundary exists in all the samples. The relative content of the T phase increases due to the Nb^{5+} doping. The ceramics show dense microstructures with mean grain sizes around 1–2 μm. The changes of dielectric constant and dielectric loss as a function of temperature for the unpoled and poled samples were compared. Two dielectric anomalies appear on the dielectric curves around the temperatures denoted as T_{RE} and T_m. With the increase of Nb^{5+} amount, the values of T_{RE} decrease and T_m increase. The Nb^{5+}-doped ceramics exhibit better temperature stability of dielectric constant during a wide high-temperature window. The polarization hysteresis (P–E) loops change from typical ferroelectric loops for the sample with $x = 0$ to constricted P–E loops with increasing Nb^{5+} amount. The ceramic with $x = 0.03$ shows a maximum strain (S_{max}) of 0.55% and piezoelectric strain constant (d_{33}^*) of 675 pm/V.

1 Introduction

$(Bi_{0.5}Na_{0.5})_{0.94}Ba_{0.06}TiO_3$ (BNBT)-based piezoelectric ceramics, which have a tetragonal (T)–rhombohedral (R) morphotropic phase boundary (MPB), have been widely explored [1, 2]. Many studies have focused on the doping of ions into BNBT-based ceramics to improve their electrical properties. The dopants can greatly affect structure and electrical behavior of the BNBT-based ceramics. Li et al. reported that the doping of La^{3+} into the A-site of BNBT disrupts dominant long-range ferroelectric order of the ceramics and significantly weakens ferroelectric properties [3]. Yang et al. found that the doping of La^{3+} into BNBT causes a decrease in grain sizes of the ceramics and improves dielectric breakdown strength [4]. Wang et al. reported that the co-doping of Ce^{4+} and La^{3+} into BNBT greatly improves their piezoelectric and dielectric constants [5]. Jing et al. studied structure, dielectric, and piezoelectric properties of $(Na_{0.47}Bi_{0.47}Ba_{0.06})_{0.95}Ca_{0.05}TiO_3$ and $(Na_{0.47}Bi_{0.47}Ba_{0.06})_{0.95}Sr_{0.05}TiO_3$ ceramics, in which the Ca^{2+} and

Address correspondence to E-mail: lianhanli@163.com

https://doi.org/10.1007/s10854-020-04660-5

Sr^{2+} have the same electric charge and different radii, and found that the average ionic radii of the A-site cations in the ABO_3 structure are important in affecting structure and electrical properties of BNBT-based ceramics [6]. The dopants into the B-site of BNBT are also important to tune electrical properties of the ceramics. Wang et al. reported that the doping of Zr^{4+} into $(Na_{0.47}Bi_{0.46}Ba_{0.06}K_{0.01})(Nb_{0.02}Ti_{0.98})O_3$ causes a decrease in dielectric constant and decrement of ferroelectric properties of the ceramics [7]. The doping of Fe^{3+} into $0.94Bi_{0.5}Na_{0.5}TiO_3$-$0.06BaTiO_3$ induces more obvious diffusion character of the phase transition around Curie temperature, which was suggested to be related to the formation of oxygen vacancies [8]. Wang et al. found that the Fe^{3+} doping into $(Bi_{0.5}Na_{0.4}K_{0.1})Ti_{0.98}Fe_{0.02}O_{3-\delta}$ reduces dielectric constant and depolarization temperature of the ceramics [9]. The doping of Co^{3+} into $0.8Bi_{0.5}$-$Na_{0.5}TiO_3$–$0.2Bi_{0.5}K_{0.5}TiO_3$ promotes grain growth, increases electric conductivity, and weakens piezoelectric properties [10]. Oxygen vacancies can always be introduced into the lattice if the cations with the electric charge lower than that of Ti^{4+} are doped into the B-site (as commonly be called hard doping). The hard doping helps increasing electromechanical behavior of the piezoelectric materials. If the cations with the electric charge higher than + 4 are introduced into the B-site, the piezoelectricity and ferroelectricity properties of the ceramics should also be changed.

The radii of Nb^{5+} and Ti^{4+} are 0.64 Å and 0.605 Å in the case of coordination number (CN) 6, respectively [11]. The similar radii between Nb^{5+} and Ti^{4+} imply that Nb^{5+} can be doped into the Ti^{4+} site. Chauhan et al. reported that the substitution of Nb^{5+} for Ti^{4+} improves piezoelectricity and ferroelectricity of the $Bi_{0.5}Na_{0.25}K_{0.25}Nb_{0.015}Ti_{0.975}O_3$ ceramics [12]. Zhang et al. studied local lattice relaxation in Nb_2O_5-modified $0.94(Na_{0.5}Bi_{0.5})TiO_3$-$0.06BaTiO_3$ ferroelectrics and found that lattice relaxation destabilizes the field-induced ferroelectric phase [13]. Petnoi et al. reported that the transition temperature of Nb^{5+}-doped $(Bi_{0.5}Na_{0.5})TiO_3$ shifts to lower temperature as the Nb^{5+} content increases [14]. Shen et al. reported that the doping of Nb^{5+} into $BaTiO_3$-$(Bi_{0.5}Na_{0.5})TiO_3$ is beneficial to promote the formation of the core–shell structure and weakens dependence of dielectric properties on temperature [15]. The doping of Nb^{5+} will always introduce cation vacancies in the A-site because of higher electric charge of Nb^{5+}, which can affect electrical performance of the ceramics.

In this work, the $(Bi_{0.5}Na_{0.5})_{0.94-\delta}Ba_{0.06}Ti_{1-x}Nb_xO_3$ ceramics were obtained via solid-state sintering. Effects of Nb^{5+} doping on microstructure, phase structure, dielectric, piezoelectric, and ferroelectric behavior were studied.

2 Experimental procedure

The ceramics $(Bi_{0.5}Na_{0.5})_{0.94-\delta}Ba_{0.06}Ti_{1-x}Nb_xO_3$ (denoted as BNBTN/x, x = 0, 0.01, 0.02, 0.03, 0.04, 0.05) were prepared by means of a solid-state sintering method. The raw powders are $BaCO_3$ (≥ 99.0%), Na_2CO_3 (≥ 99.8%), Bi_2O_3 (≥ 98.9%), TiO_2 (≥ 98.0%), and Nb_2O_5 (≥ 99.99%). After being baked at 120 °C for 1 day, the powders were weighed according to the compositions. The dried powders were ball milled for 1 day in a planetary milling apparatus. Then, the milled powders were calcined at 900 °C for 180 min and then ball milled again. 5 wt% PVA was added into the powders, and then green pellets with diameter 10 mm and thickness approximate 1.5 mm were pressed at 200 MPa. The PVA was burned out at 500 °C for 120 min. The sintering temperature, dwelling time, and heating/cooling rates are 1170 °C, 180 min, and 3 °C/min, respectively.

Bulk densities of the ceramics were obtained via the Archimedes method. The method for calculating weight loss of the samples during the sintering process has been clarified in the previous work [16]. Phase structure was measured via a Rigaku D/Max 2550 X-ray diffraction (XRD) apparatus. Raman spectra were obtained via an Almega-dispersive Raman spectrometer. Scanning electron microscope (SEM) images for the thermally etched ceramics were measured via a Quanta 200 SEM. The ceramics were poled at 5 kV/mm for 30 min at room temperature. Piezoelectric constant d_{33} was measured via a quasistatic d_{33} meter (ZJ-4A). Ferroelectric behavior was measured via Precision Premier II ferroelectric testing system. Dielectric properties were measured on a dielectric spectrometer (Novocontrol Concept 80).

3 Result and discussion

Figure 1 shows the SEM images of the surfaces of the thermally etched BNBTN/x ceramics. All the ceramics exhibit dense microstructures with average grain sizes around 1–2 μm. The grains and grain boundaries are clear. Almost no pores were found in the samples. The dense microstructures correspond to their high densities. The bulk densities of the BNBTN/x samples are larger than 5.75 g/cm^3 (Fig. 2). All the samples exhibit relative densities higher than 96% (theoretical density of $(Na_{0.5}Bi_{0.5})_{0.94}Ba_{0.06}TiO_3$ 5.98 g/cm^{-3} roughly used for all the compositions [17]), implying that the ceramics were well sintered at 1170 °C. Weight loss of the ceramics during sintering is shown in Fig. 2. It is found that there appears an increase in the weight loss with the increase of Nb^{5+} content. As mentioned above, all the samples with the different compositions were prepared using the same synthesis parameters, such as sintering temperature, dwelling time, and heating/cooling rates. So, the difference in

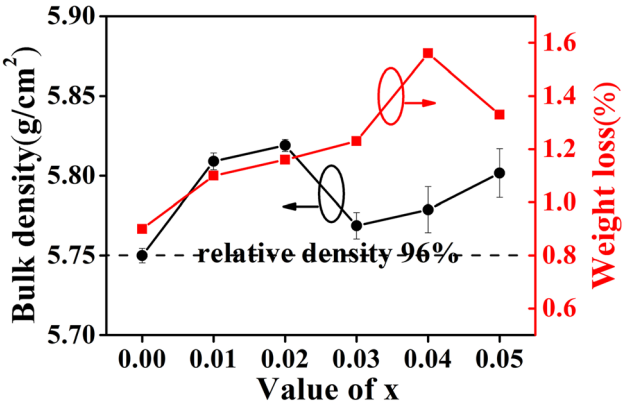

Fig. 2 Bulk densities and weight loss of the ceramics

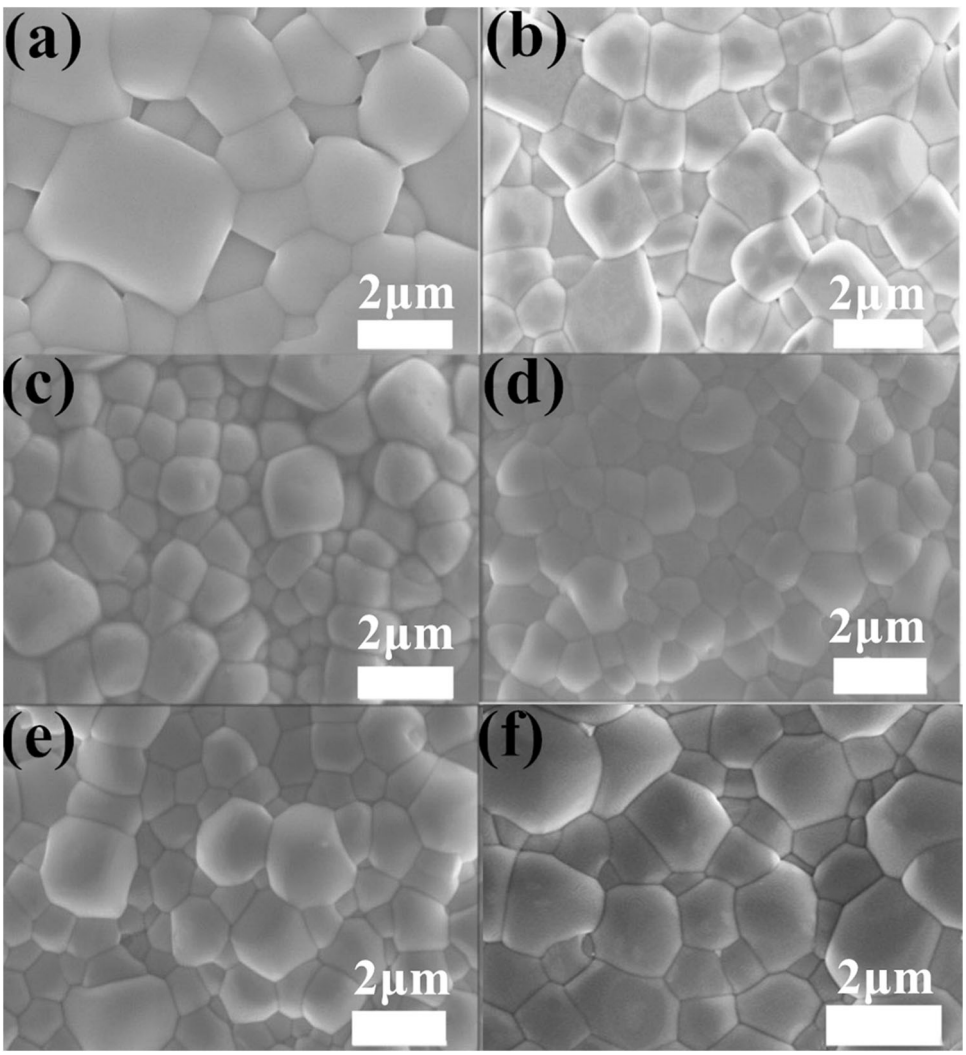

Fig. 1 SEM images of the surfaces of the thermally etched ceramics with x = 0 (**a**), x = 0.01 (**b**), x = 0.02 (**c**), x = 0.03 (**d**), x = 0.04 (**e**), x = 0.05 (**f**)

weight loss of the samples should be caused by the difference in the Nb^{5+} amounts. It is well known that the doping of Nb^{5+} into the B-site will cause cation vacancies in the A-site, as shown by the Kröger–Vink equation:

$$\begin{aligned} &3/2Nb_2O_5 \xrightarrow{(Bi_{0.5}Na_{0.5})_{0.94}Ba_{0.06}TiO_3} 3Nb_{Ti}^{\cdot} + V_{Bi}^{///} \\ &\quad + 1/2Bi_2O_3(\uparrow) \\ &1/2Nb_2O_5 \xrightarrow{(Bi_{0.5}Na_{0.5})_{0.94}Ba_{0.06}TiO_3} Nb_{Ti}^{\cdot} + V_{Na}^{/} \\ &\quad + 1/2Na_2O(\uparrow) \end{aligned} \quad (1)$$

According to the equation, more cation vacancies including $V_{Bi}^{///}$ and $V_{Na}^{/}$ will be introduced as more Nb^{5+} cations are doped into the Ti^{4+} sites, which should be responsible for the increase in weight loss of the samples. In addition, the sample with $x = 0.05$ shows a slight decrease in weight loss, which may be related to the formation of a secondary phase in the sample, as shown in Fig. 3a.

The XRD curves of the ceramics are shown in Fig. 3a. The samples exhibit typical diffraction peaks of the perovskite structure. For the sample with $x = 0.05$, there appears another peak around 29°, implying a secondary phase exists in the ceramic. The peak position of the secondary phase is in accordance to that of the XRD peak with the largest intensity for Nb_2O_5 (International Centre for Diffraction Data, No. 32-0710). It is reasonable to infer that the secondary phase is related to the excess Nb_2O_5. It is well known that the rhombohedral–tetragonal MPB exists in the ceramics with the composition of $(Bi_{0.5}Na_{0.5})_{0.94}$-$Ba_{0.06}TiO_3$ [18, 19]. For the MPB composition, three XRD peaks exist around 46° corresponding to the diffraction planes $(002)_T$, $(200)_T$, and $(200)_R$ in which R and T represent the rhombohedral phase and tetragonal phase, respectively [20]. The detail of the XRD peaks in the 2θ range from 46° to 47° is exhibited in Fig. 3b. The XRD peaks around 46° of the $x = 0$ and $x = 0.01$ ceramics are asymmetric obviously. With further increasing the Nb^{5+} amount, the peaks split remarkably. The peaks can be well fitted into three peaks. Relative amount of the tetragonal phase (T%) can be estimated via the equation:

$$T\% = [S_{(002)T} + S_{(200)T}]/[S_{(200)R} + S_{(002)T} + S_{(200)T}], \quad (2)$$

in which $S_{(200)R}$, $S_{(002)T}$, and $S_{(200)T}$ are area values of the $(200)_R$, $(002)_T$, and $(200)_T$ diffraction peaks, respectively. The obtained T% values are 45%, 48%, 50%, 52%, 54%, and 57% for the ceramics with $x = 0$, 0.01, 0.02, 0.03, 0.04, and 0.05, respectively. Compared to BNBTN/0, the Nb^{5+} doping induces an increment of T%. In addition, the XRD peaks move toward lower 2 theta direction. For example, the 2θ values of the $(200)_R$ peaks for the ceramics with $x = 0$, 0.01, 0.02, 0.03, 0.04, and 0.05 are 117°, 103°, 101°, 100°, 98°, and 97°, respectively. It is known that the radius of Nb^{5+} with CN = 6 is 0.64 Å, and that of Ti^{4+} in the case of CN = 6 is 0.605 Å [11]. The substitution of Nb^{5+} for Ti^{4+} causes enlargements of the unit cell because of the larger radius of Nb^{5+}, contributing to the shift of the peaks. In addition, the doping of Nb^{5+} into the B-site will cause cation vacancies in the A-site (Eq. 1). The formation of point defects in the ceramics induces lattice distortion, also contributing to the shift of the XRD peaks.

Figure 4 shows the result of Raman spectroscopy. All the samples show similar curves. The curves can

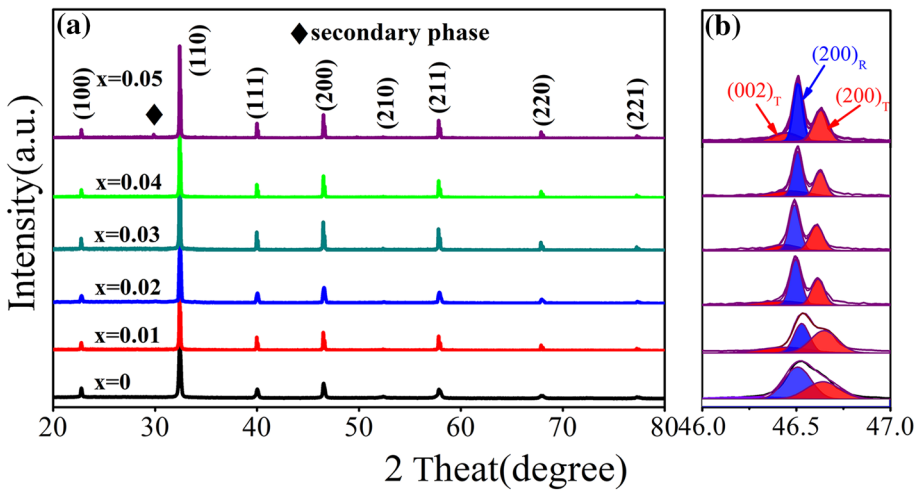

Fig. 3 XRD curves of the ceramics (**a**); XRD fitting patterns around 46°

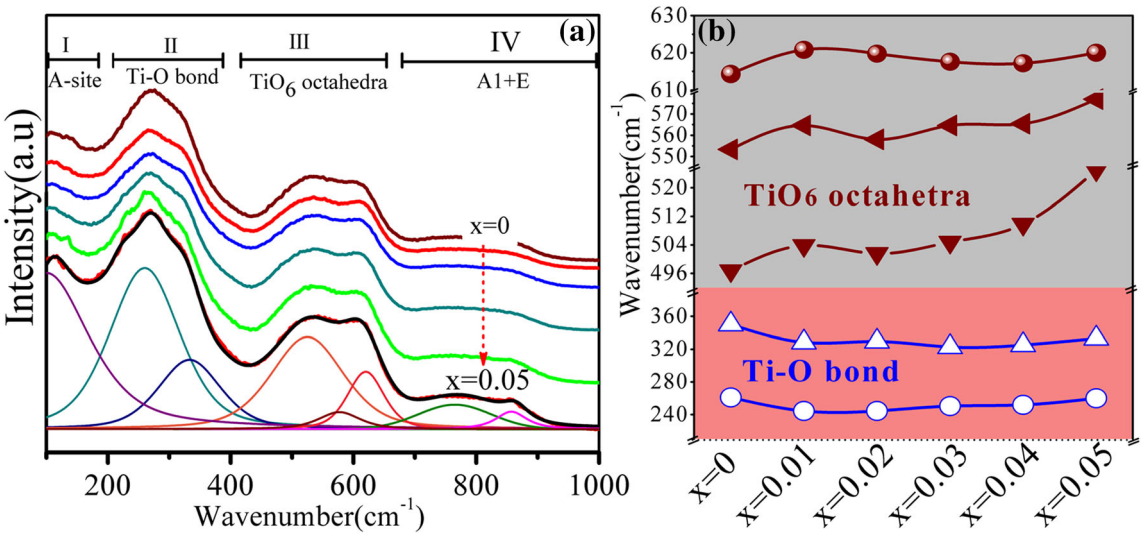

Fig. 4 Raman spectra of the ceramics (**a**); the typical result of spectral deconvolution for the ceramic with $x = 0.05$ according to the Gaussian–Lorentzian modes via a best-fitting algorithm is shown in the bottom in **a**. Typical positions of the Raman vibration modes corresponding to Ti–O bond and TiO_6 octahedra (**b**)

be divided into four regions, i.e., Region I, Region II, Region III, and Region IV, which are associated with the vibration modes of A-site, Ti–O bond, TiO_6 octahedra, and A_1+E overlapping band, respectively [21]. According to the eight Gaussian–Lorentzian modes [6], spectral deconvolution in the Raman spectroscopy was performed, and the typical positions of the Raman vibration modes corresponding to Ti–O bond and TiO_6 octahedra are shown in Fig. 4b. It is obvious that two peaks exist in Region II. The splitting of the peaks locating in Region II is often regarded as a sign of the coexistence of rhombohedral and tetragonal phases [22]. The two peaks corresponding to Ti–O bond imply coexistence of the rhombohedral and tetragonal phases, which are in accordance with the XRD result (Fig. 3b). The positions of the two peaks corresponding to Ti–O bond shift toward lower wavenumber slightly with the increase of Nb^{5+} amount (Fig. 4b), suggesting the variation in B–O bond (B = Ti/Nb) due to the doping of Nb^{5+}. For TiO_6 octahedra vibration mode, the Nb^{5+}-doped ceramics exhibit higher wavenumber value compared with the ceramic with $x = 0$. In addition, the positions of the two peaks around 500 cm^{-1} and 620 cm^{-1} tend to shift together with the increase of x. For example, the distance between the two peaks for the ceramic with $x = 0$ is 61 cm^{-1}, while that for the ceramic with $x = 0.05$ is 43 cm^{-1}. The substitution of Nb^{5+} for Ti^{4+} causes lattice distortion, inducing change of TiO_6 octahedra vibration mode. The Raman result further demonstrates the entrance of Nb^{5+} into the BNBT lattice.

Figure 5 shows variation of dielectric loss (tanδ) and dielectric constant (ε_r) of the unpoled samples with changing temperature (T). There are two dielectric anomalies for all the samples, which are denoted as T_{RE} and T_m, respectively. T_{RE} is the temperature at which ε_r values at various frequencies begin to merge together. When the temperature is lower than T_{RE}, ε_r has an obvious dependence on frequency, and ε_r at high frequency is less than that at low frequency. When temperature is higher than T_{RE}, the ε_r values at different frequencies are very close, and the frequency dispersion tends to disappear. The temperature corresponding to the maximum permittivity (ε_m) is denoted as T_m. The similar dielectric behavior was always observed in BNBT-based ceramics [6, 8, 20]. The dielectric anomalies around T_{RE} and T_m have been suggested to be associated with thermal evolution of polar nanoregions with the different symmetries [23, 24]. The values of T_{RE}, T_m, and ε_m of the ceramics are shown in Table 1. Here, the T_{RE} values were determined via the temperatures at which the difference in dielectric constant at 1 kHz and 100 kHz, i.e., $\Delta\varepsilon_r = \varepsilon_{r\ (1\ kHz)} - \varepsilon_{r\ (100\ kHz)}$, is minimum [25]. As the Nb^{5+} amount increases from $x = 0$ to $x = 0.05$, T_{RE} decreases from 217 to 171 °C, T_m changes from 272 to 297 °C, and ε_m changes from 6282 to 2880. The broadening of temperature window ($\Delta T = T_m - T_{RE}$) between T_{RE} and T_m as well as

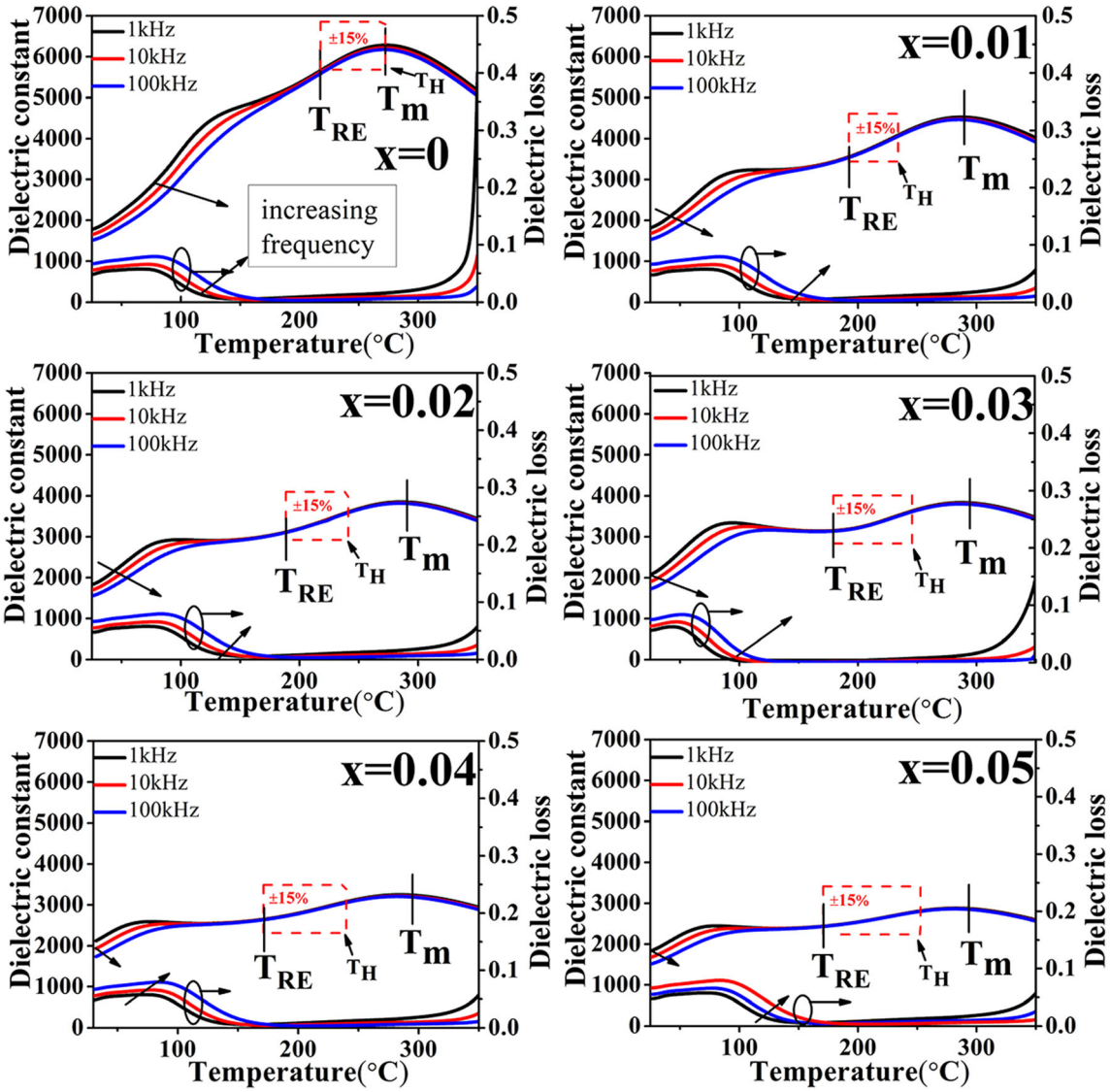

Fig. 5 Dielectric constant and dielectric loss of the unpoled ceramics as a function of temperature

Table 1 Dielectric properties and piezoelectric constant (d_{33}) of the BNBTN/x ceramics

Samples	T_{RE} (°C)	T_m (°C)	ε_m	ΔT (°C)	$\Delta\varepsilon_r$	T_d (°C)	d_{33} (pC/N)
$x = 0$	217	272	6282	55	627	101	123
$x = 0.01$	192	286	4529	94	978	54	138
$x = 0.02$	188	289	3852	101	738	41	110
$x = 0.03$	179	292	3836	113	726	–	13
$x = 0.04$	173	295	3248	122	592	–	–
$x = 0.05$	171	297	2880	126	439	–	–

$\Delta T = T_m - T_{RE}$ shows temperature window between T_m–T_{RE}. $\Delta\varepsilon_r$ is difference in dielectric constant between the temperatures T_{RE} and T_m

decrease in ε_m improves high-temperature stability of ε_r. The ε_r values at T_{RE} are 5655, 3551, 3114, 3110, 2656, and 2441 for the ceramics with x = 0, 0.01, 0.02, 0.03, 0.04, and 0.05, respectively. Those at T_m are 6282, 4529, 3852, 3836, 3248, and 2880 for BNBTN/0, BNBTN/0.01, BNBTN/0.02, BNBTN/0.03, BNBTN/0.04, and BNBTN/0.05, respectively. The differences in ε_r values at the temperatures between T_{RE} and T_m (labeled as $\Delta\varepsilon_r$) are 627, 978, 738, 726, 592, and 439 for the ceramics with x = 0, 0.01, 0.02, 0.03, 0.04, and 0.05, respectively (Table 1). In addition, the temperature coefficient of capacitance (TCC) is also applied to evaluate the temperature window for temperature stability of ε_r. Here, TCC is defined as

$$TCC = (\varepsilon_{r,H} - \varepsilon_{r,L})/\varepsilon_{r,L} \leq 15\%, \quad (3)$$

in which $\varepsilon_{r,L}$ is dielectric constant at the temperature T_{RE} and $\varepsilon_{r,H}$ is dielectric constant at a given higher temperature T_H. For the temperature T_H, the TCC value is equal to 15%. So, a higher T_H corresponds to a wider temperature window with TCC ≤ 15%, implying better temperature stability of ε_r. The temperature window for TCC ≤ 15% is also depicted in Fig. 5. The window values between T_H and T_{RE} are 55 °C, 42 °C, 50 °C, 65 °C, 74 °C, and 80 °C for the ceramics with x = 0, 0.01, 0.02, 0.03, 0.04, and 0.05, respectively. The ceramics with high Nb^{5+} amounts exhibit wide-temperature window, which is advantageous for preparing high-temperature ceramic capacitors.

The poled samples with x = 0, 0.01, and 0.02 show high d_{33} values between 110 and 138 pC/N at room temperature (Table 1). The x = 0.03 ceramic exhibits a low d_{33} of 13 pC/N. For the higher doping amounts of Nb^{5+}, no d_{33} was observed at room temperature, implying depolarization behavior at room temperature. The curves of tanδ and ε_r of the poled samples are plotted in Fig. 6. Compared to the unpoled counterparts, a new dielectric anomaly appears on the curves of the poled samples with $x \leq 0.02$. The new anomaly locates at the temperature denoted as T_d. At T_d, ε_r increases suddenly, and tanδ exhibits a sharp peak. T_d is always used to determine depolarization temperature [26–28]. Below T_d, long-range ferroelectric order exists in the ceramics due to the electric poling. As temperature rises above T_d, the long-range order will be broken, corresponding to depolarization [28]. When temperature is lower than T_d, the ε_r values of the poled samples are smaller than those of the unpoled counterparts at a given frequency and temperature. The phenomenon can be explained as follows. On one hand, the strong electric field during the poling process can reorient space charges, defect dipoles in the ceramics, and freeze them. The electric field for measuring dielectric spectra is weaker than that for poling the samples, which cannot activate the space charges and cannot reorient the defect dipoles. So, the decreased contribution from these factors causes decrease in dielectric constant [29]. On the other hand, compared to the unpoled samples, domain wall densities of the poled samples are reduced due to the electric poling, which also contribute to reduction in dielectric constant. The T_d values of the ceramics BNBTN/0, BNBTN/0.01, and BNBTN/0.02 are 101 °C, 54 °C, and 41 °C, respectively. The doping of Nb^{5+} causes a decrease in depolarization temperature. For the ceramics with $x \geq 0.03$, no T_d anomaly was found, implying that it shifts below room temperature. The phenomenon is consistent with the ferroelectric behavior as shown later.

The loops of polarization (P), strain (S), and current density (J) under as a function of measurement electric fields (E) are exhibited in Fig. 7a–f. Here, the P–E loops were measured between 50 and 80 kV/cm; S–E loops and J–E loops were recorded at the maximum electric field of 80 kV/cm. For a given sample, the P–E loops become more saturated with increasing the measurement electric fields. It is found that the shape of P–E loops is strongly affected by the content of Nb^{5+}. The ceramics with x = 0, 0.01, and 0.02 display typical P–E loops and butterfly-shaped S–E loops. Two peaks appear on the J–E loops, demonstrating ferroelectric character. With further increasing Nb^{5+} content, the P–E loops tend more pinched. The values of maximum polarization (P_m), remnant polarization (P_r), and coercive filed (E_c) of the ceramics under 80 kV/cm are shown in Fig. 7g. The polarization and E_c values decrease with increasing Nb^{5+} content, indicating destruction of long-range ferroelectric order with the doping of Nb^{5+}. In the case of $x \geq 0.03$, the P_r values are obviously decreased compared to the samples with $x < 0.03$. The S–E loops gradually change from butterfly shape to horn shape, accompanied by a decrease in negative strain. At the same time, there appear four peaks on the J–E curves. These characteristics suggest disorder of ferroelectric phase in the ceramics with the higher Nb^{5+} amounts caused by the Nb^{5+} doping and appearance of ergodic relaxation phase [30, 31], which is in good agreement with the change of T_d in dielectric behavior.

The formation of cation vacancies in the ceramics should also affect their dielectric and ferroelectric behaviors. As mentioned above, the doping of Nb^{5+} into the B-site will cause cation vacancies in the A-site (Eq. 2). In order to detect effect of cation vacancies, a typical composition of x = 0.01 was chosen, and excess $(Bi_{0.5}Na_{0.5})^{2+}$ ions were added into the composition to compensate cation vacancies. The excess $(Bi_{0.5}Na_{0.5})^{2+}$ amount was calculated to be δ = 0.015 according to the molecular formula $(Bi_{0.5}Na_{0.5})_{0.94-\delta}Ba_{0.06}Ti_{1-x}Nb_xO_3$. The obtained samples are noted as

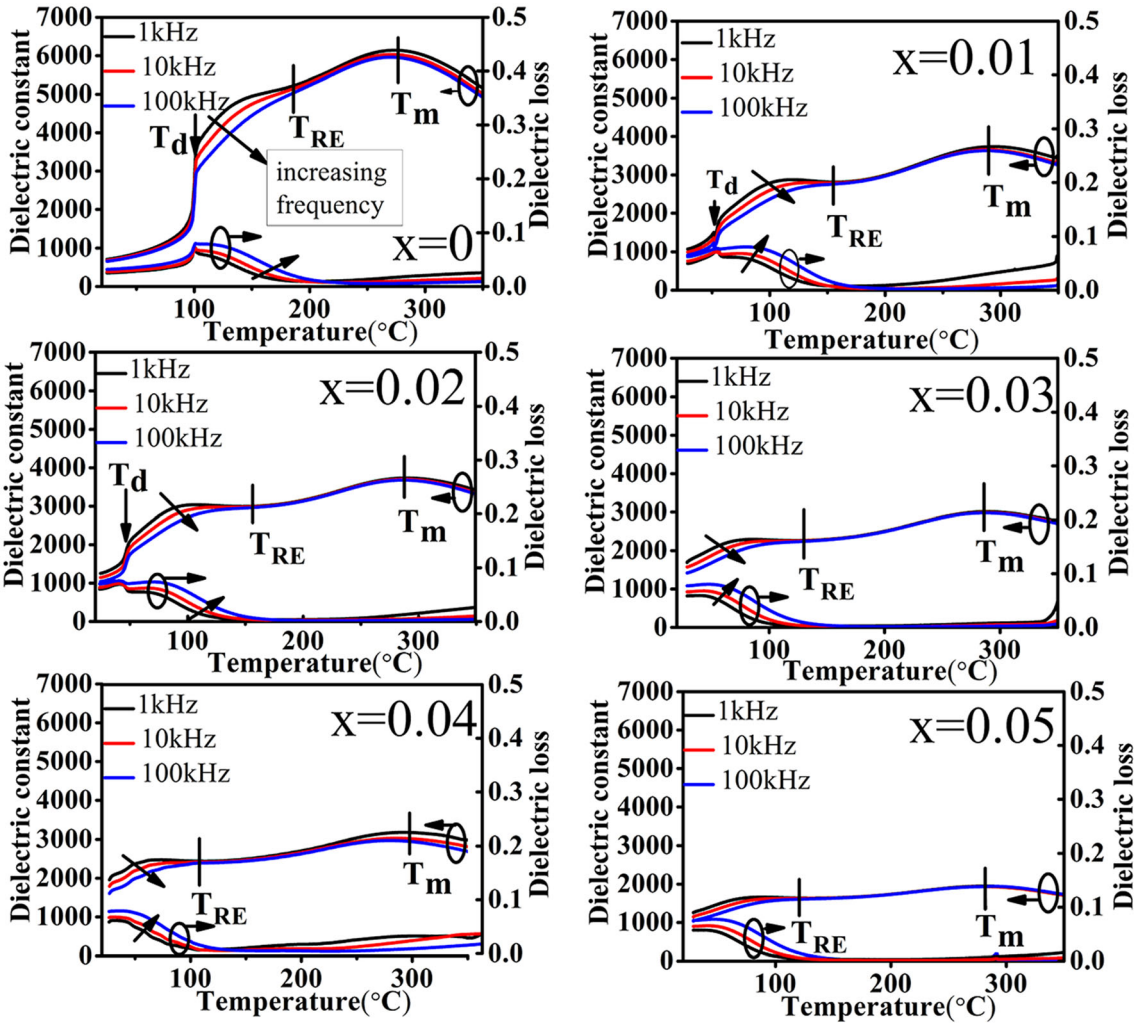

Fig. 6 Dielectric constant and dielectric loss of the poled ceramics as a function of temperature

BNBTN/0.01 + δBN. The *P*–*E* loops of BNBTN/0.01 + δBN and BNBTN/0.01 recorded at 70 kV/cm are compared in Fig. 8. The ceramic BNBTN/0.01 + δBN shows the P_m, P_r, and E_c values of 24.3 μC/cm^2, 18.6 μC/cm^2, and 33.6 kV/cm, respectively. The corresponding values for BNBTN/0.01 are 39.6 μC/cm^2, 32.8 μC/cm^2, and 27.5 kV/cm, respectively. The addition of excessive $(Na_{0.5}Bi_{0.5})^{2+}$ reduces polarization and increases coercive field. The inset in Fig. 8 shows variation of ε_r and tanδ as a function of temperature measured at 1 kHz for the poled BNBTN/0.01 and BNBTN/0.01 + δBN ceramics. Via the dielectric spectra, it is found that the adding of excess $(Na_{0.5}Bi_{0.5})^{2+}$ ions increases depolarization temperature T_d from 55 °C for BNBTN/0.01 to 65 °C for BNBTN/0.01 + δBN. As has been well known, cation vacancies always facilitate improving ferroelectric behavior, i.e., increasing polarization and decreasing coercive field [12]. In addition, depolarization temperatures for BNBT-based ceramics are related to point defects. Qiao et al. reported that point defects can affect depolarization temperature and cation vacancies facilitate decreasing T_d [2]. Compared to BNBTN/0.01, BNBTN/0.01 + δBN exhibits increased T_d, decreased polarization, and increased E_c, which are in accordance to the reduced amount of cation vacancies in BNBTN/0.01 + δBN due to the compensation of $(Na_{0.5}Bi_{0.5})^{2+}$. Via these results, it is reasonable to expect important effect of cation vacancies in the BNBTN/*x* ceramics on dielectric and ferroelectric properties.

Change of unipolar strain (S_u) as a function of electric field is shown in Fig. 9a, and the unipolar

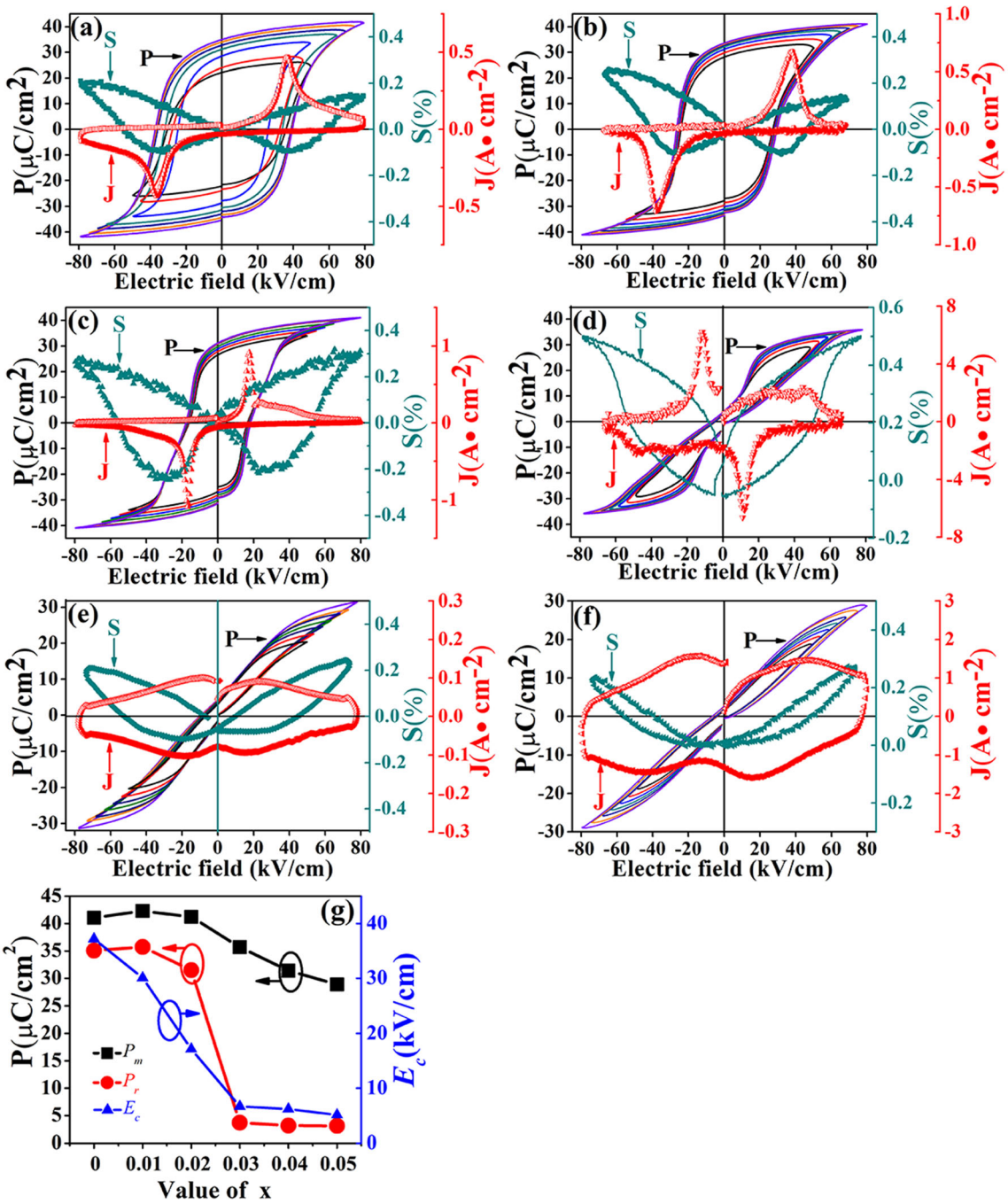

Fig. 7 The *P*–*E* loops measured at electric fields between 50 and 80 kV/cm, *S*–*E* loops and *J*–*E* loops measured at 80 kV/cm for the ceramics with $x = 0$ (**a**), $x = 0.01$ (**b**), $x = 0.02$ (**c**), $x = 0.03$ (**d**), $x = 0.04$ (**e**), $x = 0.05$ (**f**). The measurement frequency is 1 Hz. The values of E_c, P_m, and P_r measured at 80 kV/cm are shown in **g**

strain values at $E_{max} = 80$ kV/cm (S_{max}) and corresponding piezoelectric strain constant $d_{33}^* = S_{max}/E_{max}$ values are shown in Fig. 9b. It is found that S_{max} increases first and then decreases as the Nb^{5+} content increases. The ceramic BNBTN/0.03 exhibits the maximum unipolar strain 0.55%. The change of d_{33}^* with the increase in the Nb^{5+} amount is same as that of S_{max}. In general, strain in the ceramics is associated with various factors, such as lattice distortion, point defects, phase structure, destabilization of the ferroelectric phase, etc. As demonstrated via the XRD and Raman results, the doping of Nb^{5+} causes lattice

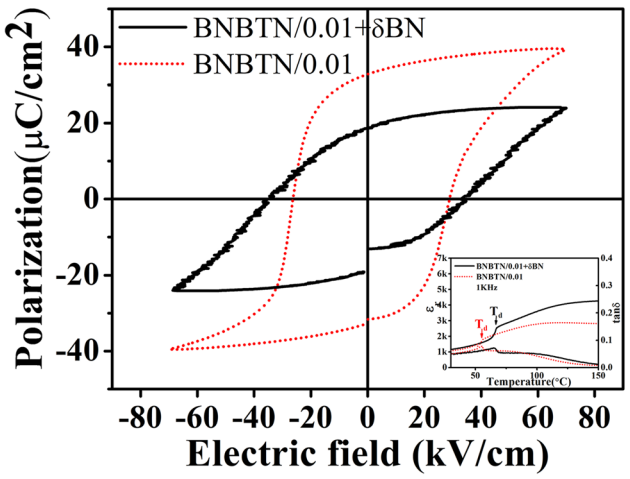

Fig. 8 *P–E* loops of the ceramics BNBTN/0.01 + δBN and BNBTN/0.01 measured at 70 kV/cm. The inset shows the ε_r and tanδ as a function of temperature measured at 1 kHz between room temperature and 150 °C for the poled BNBTN/0.01 + δBN and BNBTN/0.01 ceramics

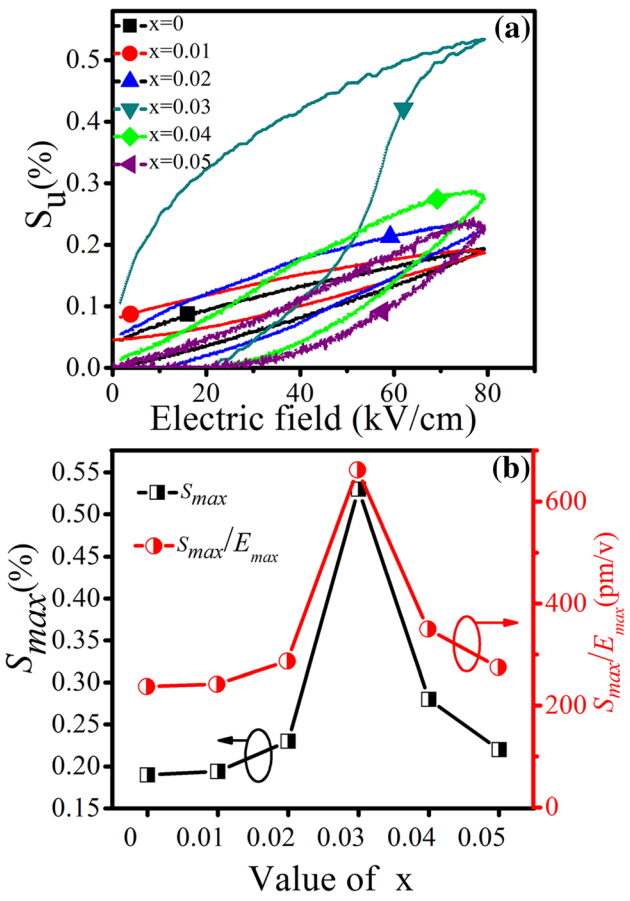

Fig. 9 Unipolar strain curves as a function of electric field (**a**). The maximum unipolar strain (S_{max}) values at 80 kV/cm and the corresponding d_{33}^* values (**b**)

distortion and variation in relative amount of the rhombohedral/tetragonal phase (Figs. 3, 4). Furthermore, the doping can also cause cation vacancies in the A-site (Eq. 1). In addition, the very slim *P–E* loops accompanied by significant reduction in polarization (Fig. 7) as well as no T_d peak on the dielectric spectra (Fig. 6) for the ceramic with $x = 0.03$ suggests the disruption of the long-range ferroelectric order caused by the Nb^{5+} doping. It is known that the destabilization of the long-range ferroelectric order was always accompanied by enhancement in the strain behavior [32]. All of these factors should contribute to the change in strain and d_{33}^* as a function of Nb^{5+} amount. As is well known, superior strain response plays important role in actuators. Wang et al. showed that $0.715Bi_{0.5}Na_{0.5}TiO_3$–$0.065BaTiO_3$–$0.22SrTiO_3$ exhibits $S_{max} = 0.2\%$ and $d_{33}^* = 490$ pm/V [33]. Liu et al. reported that $(1-x)(0.8Na_{0.5}Bi_{0.5}TiO_3$–$0.2K_{0.5}Bi_{0.5}TiO_3)$-$xSrTiO_3$ has $S_{max} = 0.3\%$ and $d_{33}^* = 500$ pm/V [21]. Zhao et al. exhibited $S_{max} = 0.13\%$ and $d_{33}^* = 448$ pm/V for the (K,Na)NbO_3-based ceramics [34]. Here, we found that BNBTN/0.03 shows the S_{max} as high as 0.55% and d_{33}^* as high as 675 pm/V, implying excellent strain performance.

4 Conclusions

The dense BNBTN/x ceramics were successfully obtained by means of a conventional sintering method. The $x < 0.05$ ceramics show pure phase, while a secondary phase exists in the $x = 0.05$ sample. The relative amounts of the tetragonal phase are 45%, 48%, 50%, 52%, 54%, and 57% for the ceramics with $x = 0$, 0.01, 0.02, 0.03, 0.04, and 0.05, respectively. For the ceramics with $x = 0$, 0.01, 0.02, 0.03, 0.04, and 0.05, the T_{RE} values are 217 °C, 192 °C, 188 °C, 179 °C, 173 °C, and 171 °C, respectively, and the T_m values are 272 °C, 286 °C, 289 °C, 292 °C, 295 °C, and 297 °C, respectively. The ε_r values exhibit excellent temperature stability for the ceramics with the high Nb^{5+} amounts. The doping of Nb^{5+} causes a decrease in T_d, which are 101 °C, 54 °C, and 41 °C for $x = 0$, 0.01, and 0.02, respectively. For the ceramics with $x \geq 0.03$, T_d decreased below room temperature. The *P–E* loops change from typical ferroelectric loops for BNBTN/0 to constricted *P–E* loops for the samples with $x \geq 0.03$, indicating disruption of the long-range ferroelectric order caused by the Nb^{5+} doping. With the increase in Nb^{5+} amount from $x = 0$ to $x = 0.05$,

the E_c value decreases from 37.2 kV/cm to 5.1 kV; the P_m value decreases from 41.1 to 28.9 μC/cm^2; and the P_r value decreases from 35.1 to 3.1 μC/cm^2. The BNBTN/0.03 ceramic shows the maximum unipolar strain S_{max} = 0.55% and d_{33}^* = 675 pm/V.

Acknowledgements

This work was supported in part by the National Natural Science Foundation of China (No. 51972202).

References

1. Z. Wang, J. Wang, X. Chao, L. Wei, B. Yang, D. Wang, Z. Yang, J. Mater. Sci. Mater. Electron. **27**, 5047 (2016)
2. X.S. Qiao, X.M. Chen, H.L. Lian, W.T. Chen, J.P. Zhou, P. Liu, J. Am. Ceram. Soc. **99**, 198 (2016)
3. F.F. Li, Y.F. Liu, Y.N. Lyu, Y.H. Qi, Z.L. Yu, C.G. Lu, Ceram. Int. **43**, 106 (2017)
4. Y. Yang, H. Wang, L.N. Bi, Q.J. Zheng, G.F. Fan, W.J. Jie, D. Lin, J. Eur. Ceram. Soc. **39**, 3051 (2019)
5. X.X. Wang, H.L.W. Chan, C.L. Choy, Appl. Phys. A **80**, 333 (2005)
6. R.Y. Jing, X.M. Chen, H.L. Lian, X.S. Qiao, X.J. Shao, J.P. Zhou, J. Eur. Ceram. Soc. **38**, 3111 (2018)
7. J. Wang, X.M. Chen, X.M. Zhao, X.X. Liang, X. Liu, P. Liu, J. Electroceram. **32**, 332 (2014)
8. X.M. Chen, X.X. Gong, T.N. Li, Y. He, P. Liu, J. Alloys Compd. **507**, 535 (2010)
9. T. Wang, X.M. Chen, Y.Z. Qiu, Ferroelectrics **510**, 161 (2017)
10. T. Wang, X.M. Chen, Y.Z. Qiu, H.L. Lian, W.T. Chen, Mater. Chem. Phys. **186**, 407 (2017)
11. R.D. Shannon, Acta. Crystallogr. A **32**, 751 (1976)
12. V. Chauhan, S.K. Ghosh, A. Hussain, S.K. Rout, J. Alloys Compd. **674**, 413 (2016)
13. H.W. Zhang, H. Yan, X.B. Li, H.S. Luo, Scr. Mater. **156**, 32 (2018)
14. N. Petnoi, P. Bomlai, S. Jiansirisomboon, A. Watcharapasorn, Ceram. Int. **39**, S113 (2013)
15. Z.B. Shen, X.H. Wang, D.S. Song, L.T. Li, Adv. Appl. Ceram. **115**, 435 (2016)
16. Z.D. Yu, X.M. Chen, H.L. Lian, Q. Zhang, W.X. Wu, J. Mater. Sci. Mater. Electron. **29**, 19043 (2018)
17. X.M. Chen, H.Y. Ma, W.Y. Pan, M. Pang, P. Liu, J.P. Zhou, Mater. Chem. Phys. **132**, 368 (2012)
18. N.S. Zhao, H.Q. Fan, X.H. Ren, S. Gao, J.W. Ma, Y.G. Shi, Ceram. Int. **44**, 571 (2018)
19. R. Dittmer, K.G. Webber, E. Aulbach, W. Jo, X.L. Tian, J. Rödel, Acta Mater. **61**, 1350 (2013)
20. Y.Z. Qiu, X.M. Chen, H.L. Lian, J.P. Ma, W.Q. Ouyang, Mater. Chem. Phys. **202**, 197 (2017)
21. X. Liu, J.W. Zhai, B. Shen, F. Li, Y. Zhang, P. Li, B.H. Liu, J. Eur. Ceram. Soc. **37**, 1437 (2017)
22. E. Aksel, J.S. Forrester, H.M. Foronda, R. Dittmer, J. Appl. Phys. **112**, 054111 (2012)
23. J.D. Zang, M. Li, D.C. Sinclair, W. Jo, J. Am. Ceram. Soc. **97**, 1523 (2014)
24. A. Khesro, D. Wang, F. Hussain, D.C. Sinclair, A. Feteira, I.M. Reaney, Appl. Phys. Lett. **109**, 142907 (2016)
25. R.Y. Jing, X.M. Chen, J.P. Ma, H.L. Lian, W.T. Chen, J. Mater. Sci. **53**, 274 (2018)
26. J.U. Rahman, A. Hussain, A. Maqbool, G.H. Ryu, T.K. Song, W.J. Kim, M.H. Kim, J. Alloys Compd. **593**, 97 (2014)
27. J. Shi, W.C. Tian, X. Liu, H.Q. Fan, J. Am. Ceram. Soc. **100**, 1080 (2016)
28. W. Jo, J. Daniels, D. Damjanovic, W. Kleemann, J. Rödel, Appl. Phys. Lett. **102**, 192903 (2013)
29. X.S. Qiao, X.M. Chen, H.L. Lian, J.P. Zhou, P. Liu, J. Eur. Ceram. Soc. **36**, 3995 (2016)
30. Y. Wu, G. Wang, Z. Jiao, Y. Fan, P. Peng, X. Dong, RSC Adv. **9**, 21355 (2019)
31. T.Y. Li, X.J. Lou, X.Q. Ke, S.D. Cheng, S.B. Mi, X.J. Wang, J. Shi, X. Liu, G.Z. Dong, H.Q. Fan, Y.Z. Wang, X.L. Tan, Acta Mater. **128**, 337 (2017)
32. A. Ullah, C.W. Ahn, A. Hussain, S.Y. Lee, I. W. Kim, J. Am. Ceram. Soc. **94**, 3915 (2011)
33. F.F. Wang, M. Xu, Y.X. Tang, W. Tao, W.Z. Shi, C.M. Leung, J. Rödel, J. Am. Ceram. Soc. **95**, 1995 (2012)
34. Y. Zhao, J. Du, Z.J. Xu, Mater. Sci. Eng. B **224**, 110 (2017)